

RESEARCH ARTICLE | JULY 18 2023

X-FAST: A versatile, high-throughput, and user-friendly XUV femtosecond absorption spectroscopy tabletop instrument



Ryan Ash ; Zain Abhari ; Roberta Candela ; Noah Welke ; Jake Murawski ; S. Minhal Gardezi ; Nikhilesh Venkatasubramanian ; Muneeza Munawar ; Frank Siewert ; Andrey Sokolov ; Zachary LaDuca ; Jason Kawasaki ; Uwe Bergmann



Rev Sci Instrum 94, 073004 (2023)
<https://doi.org/10.1063/5.0146137>



View
Online



Export
Citation

CrossMark

X-FAST: A versatile, high-throughput, and user-friendly XUV femtosecond absorption spectroscopy tabletop instrument

Cite as: *Rev. Sci. Instrum.* **94**, 073004 (2023); doi: [10.1063/5.0146137](https://doi.org/10.1063/5.0146137)

Submitted: 10 February 2023 • Accepted: 25 June 2023 •

Published Online: 18 July 2023



View Online



Export Citation



CrossMark

Ryan Ash,¹ Zain Abhari,¹ Roberta Candela,¹ Noah Welke,¹ Jake Murawski,¹ S. Minhal Gardezi,¹ Nikhilesh Venkatasubramanian,¹ Muneeza Munawar,¹ Frank Siewert,² Andrey Sokolov,² Zachary LaDuca,³ Jason Kawasaki,³ and Uwe Bergmann^{1,a)}

AFFILIATIONS

¹Department of Physics, University of Wisconsin Madison, 1150 University Ave., Madison, Wisconsin 53706, USA

²Helmholtz Zentrum Berlin für Materialien und Energie, Department of Optics and Beamlines, Albert-Einstein-Str. 15, 12489 Berlin, Germany

³Department of Materials Science and Engineering, University of Wisconsin Madison, 1509 University Ave., Madison, Wisconsin 53706, USA

^{a)} Author to whom correspondence should be addressed: u Bergmann@wisc.edu

ABSTRACT

We present the X-FAST (XUV Femtosecond Absorption Spectroscopy Tabletop) instrument at the University of Wisconsin-Madison. The instrument produces femtosecond extreme ultraviolet photon pulses via high-harmonic generation in the range of 40–72 eV, as well as optical pump pulses for transient-absorption experiments. The system implements a gas-cooled sample cell that enables studying the dynamics of thermally sensitive thin-film samples. This paper provides potential users with specifications of the optical, vacuum, data acquisition, and sample cooling systems of the X-FAST instrument, along with performance metrics and data of an ultrafast laser-induced phase transition in a Ni₂MnGa Heusler thin film.

Published under an exclusive license by AIP Publishing. <https://doi.org/10.1063/5.0146137>

INTRODUCTION

Ultrafast core-level spectroscopy is a powerful technique to unveil electronic and vibrational dynamics with element specificity.^{1–5} With the recent advancements of tabletop instruments driven by high-harmonic generation (HHG),^{6,7} core-level spectroscopy in the extreme ultraviolet (XUV) and soft x-ray regions can be performed directly in the laboratory with time resolution down to attoseconds.^{8–13} These systems, along with x-ray free electron laser (XFEL) facilities, have revolutionized our capability to investigate light–matter interactions on the timescale of bond breaking, spin flips, and other electronic structure changes, and, in the case of XFELs, with atomic spatial resolution.^{14,15} Tabletop XUV and soft x-ray systems have become increasingly common in recent years and have been used to study photodissociation, strong-field ionization, wavepacket dynamics in gases,^{16–20} intersystem crossing and charge transfer dynamics in transition metal complexes,^{21–24} photoinduced dynamics in liquids,¹² and

carrier, magnetization, and lattice dynamics in condensed matter systems.^{25–29} Given these newly expanded capabilities, there is a burgeoning demand for capacity and efficiency in carrying out ultrafast core-level spectroscopy experiments. At XFEL facilities, this issue is being addressed by increasing pulse repetition rates, allowing for rapid data collection, higher sensitivity to subtle electronic structure changes, and allowing more experiments to operate simultaneously. With XUV sources, the technology is currently largely limited to labs with intimate knowledge of ultrafast laser systems and nonlinear optics, which many chemists and material scientists, who would benefit from ultrafast core-level spectroscopy, are unfamiliar with. To address these challenges, XUV user facilities such as ARTEMIS, HELIOS, and CITIUS aim to provide the general scientific community access to ultrafast core level spectroscopy experiments.^{30–32}

Here, we describe the X-FAST (XUV Femtosecond Absorption Spectroscopy Tabletop) instrument, which is in the commissioning phase of becoming a user facility for the University

of Wisconsin-Madison. We discuss the main design principles, including ease of alignment, operation simplicity, automatized data collection, and provisions for sensitive samples that are easily damaged by pump laser heating. We present the design of the X-FAST instrument, the XUV source performance, and the first data collected on an ultrafast laser-induced phase transition in a half-Heusler membrane. This paper provides readers interested in the application of this powerful emerging instrumentation with the experimental parameters, sample requirements, and operational details that will lower the barrier to using ultrafast core-level spectroscopy techniques.

EXPERIMENTAL SETUP

Optical system and XUV generation

A schematic of the X-FAST instrument is shown in Fig. 1, along with an image in Fig. 2. The entire optical and vacuum system fits on a 5×20 in. laser table. A commercial Ti:Sapphire laser system (Astrella, Coherent) providing 35 fs pulses centered at 800 nm with an average power of 7 W at a 1 kHz repetition rate is used to produce both optical pump and XUV probe pulses. A variable beam splitter in the amplifier splits the beam into pump and probe paths. Both paths have their own grating compressors to tune pulse characteristics. The optical pump beam path contains a variable attenuator, zeroth-order waveplate, and optical delay line to control the pump power, polarization, and time delay between the pump and XUV pulses. The pump beam is focused by a 75 cm fused silica plano-convex lens onto the sample position at a 7° angle relative to the XUV path. Pump wavelengths can be switched from 800 to 400 nm by including a β -barium borate (BBO) and shortpass filter to allow pumping with the second harmonic. A noncollinear optical parametric amplifier (NOPA) that is currently in the commissioning phase will allow pumping at wavelengths between 500 and 700 nm.

The 5 mJ near-infrared (NIR) driver pulse used for HHG is focused with a 75 cm fused silica plano-convex lens into a 50 cm long semi-infinite gas cell.^{33,34} This type of gas cell produces high XUV flux with looser alignment tolerances than required in other

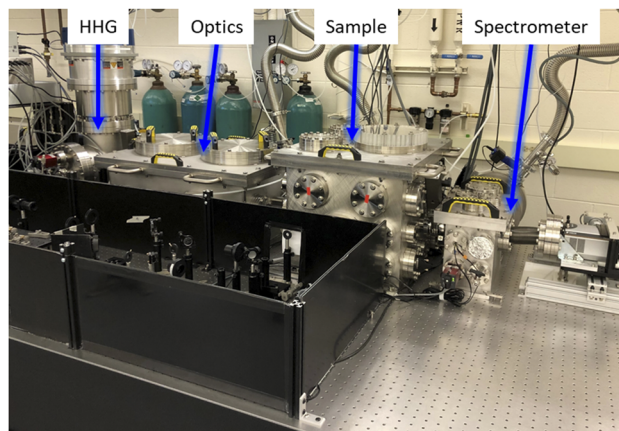


FIG. 2. Image of the X-FAST instrument. The first vacuum chamber contains the gas cell used for HHG, followed by a chamber housing filtering and focusing optics. This is followed by a sample chamber and a spectrometer chamber containing a grating and CCD detector. The optical pump path is housed on the near side of the table and routed into the sample chamber.

gas cells such as capillary waveguides.³⁵ An iris diaphragm is placed in front of the lens for fine tuning the laser pulse energy and focusing conditions.³⁶ The beam waist at the focus in the cell is $68 \pm 2 \mu\text{m}$ FWHM, yielding a maximally attainable peak intensity of $2.75 \pm 0.2 \times 10^{15} \text{ W/cm}^2$. The lens is mounted on a translation stage to control the beam focus position in the gas cell. After the gas cell, most of the driver pulse is attenuated by a silicon mirror with an 82° angle of incidence (7° offset from Brewster's angle). The mirror reflects less than 10% of the driving laser and an estimated 60%–90% between 40 and 72 eV. The silicon mirror is mounted on a water-cooled copper heat sink to reduce beam drift from thermal expansion. The rest of the NIR beam is filtered with a 100 nm Al filter (Luxel) on a push-pull mount. The diverging XUV beam is focused onto a sample position using a gold-coated toroidal mirror (ARW). The angle of incidence of the mirror is 85° , and the radii of curvature were chosen such that the source-mirror and

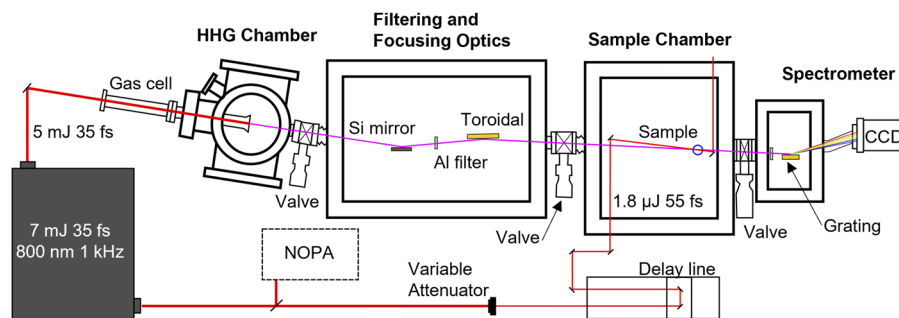


FIG. 1. Schematic of the X-FAST instrument. A single Ti:Sapphire laser drives both XUV and pump paths, which are split inside the laser amplifier by a polarizing beam splitter. 5 mJ of the laser output is used for HHG in a semi-infinite gas cell. The resulting XUV pulse is isolated with a Si mirror and Al filter, then focused with a toroidal mirror onto the sample position denoted by the blue circle. A homemade spectrometer consisting of a variable line-space grating and CCD detector collects the XUV spectrum. For transient absorption spectroscopy, the rest of the laser output is attenuated, sent through a variable delay line, and focused on the sample. A NOPA is currently in the commissioning phase.

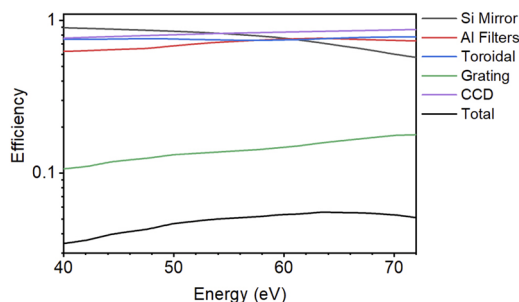


FIG. 3. Estimated reflection, transmission, and quantum efficiencies along with measured diffraction efficiency of the optical components in the XUV instrument. The overall photon into photon detected efficiency of the XUV instrument is also shown.

mirror-image distances are both 75 cm in length. The reflectivity of the mirror is $\sim 80\%$ between 40 and 72 eV. After the XUV beam has transmitted through the sample, the spectrum is collected using a homemade spectrometer consisting of a 100 nm aluminum filter, a spherical variable line space grating (Hitachi 001-0437), and an x-ray CCD detector (Newton 940) cooled to -60°C when collecting data. The grating has a flatfield focus for photon energies between 30 and 250 eV, which allows us to collect a spectral window from 33 to 80 eV with a resolution of <150 meV (in practice, the window is reduced from 40 to 72 eV from low flux and second order diffraction of photons above 66 eV).³⁷ The detector is connected to two linear actuators that control the detected energy range and position along the grating focus. The combined spectrometer efficiency is 8%–15% from 40 to 72 eV, and the estimated efficiency of detected photons vs photons produced is between 3% and 5.5%. An overview of the energy-dependent efficiencies of each optical component of the XUV instrument is shown in Fig. 3. Efficiencies for the Si mirror, Al filters, and toroidal mirror are calculated using tabulated values from the Center for X-ray Optics.³⁸ The presence of oxide coatings on the optics is not included in the efficiency estimations, and the RMS mirror surface roughness used in the calculation is 1 nm. The first order diffraction efficiency of the grating was measured at the optics beamline (PM1) reflectometer at BESSY-II,³⁹ and the CCD quantum efficiency is provided by the manufacturer. Alignment of the XUV path is performed using an NIR driving laser. Gate valves with optically transparent sapphire windows allow for the alignment of the XUV path without venting the entire vacuum system, reducing instrument downtime if realignment is required.

Vacuum system

The sub-mm attenuation length of XUV photons requires the experimental setup to operate under a vacuum. The vacuum system houses an interface to the HHG gas cell, XUV optics, and samples. It consists of four chambers: a chamber connected to the gas cell used for producing high-order harmonics; a chamber containing components to filter the NIR laser and focus the XUV beam; a chamber where the XUV and optical pump beams are directed and focused onto the sample; and a chamber with a grating and soft x-ray CCD camera. The major considerations of the vacuum system include the

total gas load from high-harmonic generation and sample cooling, the isolation of each chamber from both the other chambers and roughing lines, and interlock logic to prevent pump damage in the case of an unexpected system failure.

The primary gas load on the vacuum system is gas that escapes the semi-infinite gas cell through a laser-drilled output hole pumped out by a 1600 L/s turbomolecular pump in the first chamber. The hole is drilled through a 250 μm thick stainless-steel foil layered with two 750 μm thick cellulose acetate sheets. Using this method, pressures upward of 200 Torr can be achieved in the gas cell simultaneously with pressures below 1×10^{-3} Torr in the first vacuum chamber. Typical working gas cell pressures are between 50 and 150 Torr, with the adjacent vacuum chamber pressures between 1×10^{-4} and 5×10^{-4} Torr. Samples can be housed in a nitrogen gas cooling cell to mitigate heat introduced through optical pumping, which flows from the sample cell into the sample chamber. The nitrogen flow rate is kept at a low rate of ~ 15 SCCM and pumped from the chamber with a second 1600 l/s turbo. At this flow rate, the sample chamber's operating pressure is 1×10^{-4} Torr. Operating pressures for the optics and spectrometer chambers are 1×10^{-5} and 1×10^{-7} Torr and pumped by 800 and 1000 l/s turbos, respectively.

With gas continually flowing into our vacuum system, interlock logic is employed to isolate vacuum chambers and components in the case of a system failure. Gate valves connect each chamber and automatically shut if the pressure difference between adjacent chambers increases above 2 Torr. Similar systems are in place to close butterfly valves between the chamber and roughing lines. The electronic butterfly valves are also used to automate evacuating the vacuum system to low vacuum pressures after a chamber is vented for maintenance or sample changeover, simplifying instrument startup procedures.

Data acquisition system

The X-FAST data acquisition system is operated through a single computer running LabVIEW software, which controls sample and delay line positions, accumulation time, readout and positioning of the detector, and a shutter between the pump path and sample. Along with device control, key instrument performance diagnostics are displayed to ensure the instrument is performing properly. XUV stability is monitored by displaying the difference between the last two accumulated spectra and total integrated counts over time. Spectra are typically collected using the full vertical binning mode of the detector, assuming the dispersed energy axis lies along horizontal pixels, but a full detector image can also be acquired to display the harmonic position and ensure proper alignment between the dispersed XUV beam and the detector. An option to coarsely map a sample window is present to either find a small sample transferred to a membrane or map the thickness variation of a larger sample region.

For ground-state absorption measurements, a transmission spectrum is collected with the XUV beam passing through a sample and a reference, typically a silicon nitride membrane, on which samples are commonly deposited. The absorption spectrum is then calculated by taking the negative log of the transmittance through the sample with respect to the reference. This same principle is used to collect transient absorption data, but the sample and

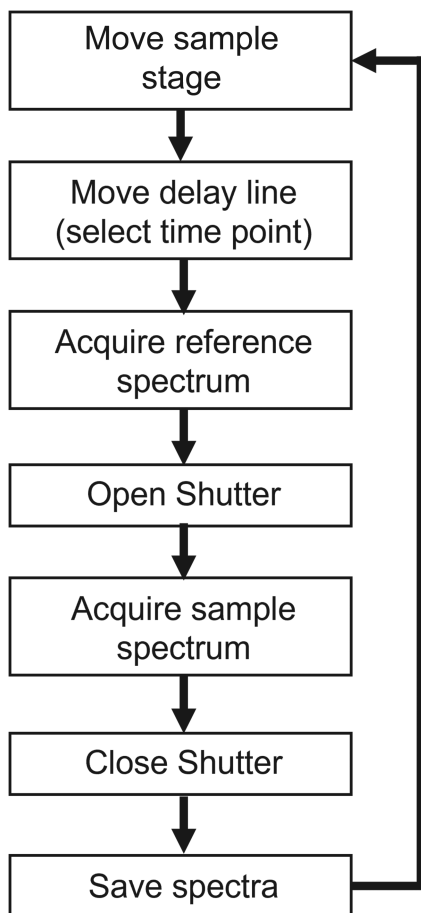


FIG. 4. Block diagram of the sequence used to collect transient absorption data.

reference spectra are in the same position while either having the pump blocked or exciting the sample, controlled using an optical shutter. The shutter is opened/closed 10 ms before/after the pump on the spectrum is acquired. An overview of the pump-probe data acquisition procedure is shown in Fig. 4. If size permits, the sample is rastered between pump-probe acquisition pairs to minimize sample damage. The time delay is also changed before each acquisition to average possible long-term power fluctuations or sample degradation across each time point. If correlations between sample rastering and time points (for example, thickness gradients) are expected, the order in which data at different timepoints is collected can be randomly scrambled. Typical acquisition loop times for pump-probe data are around 2.5 s, and 75%–80% of that time is the accumulation of photons by the detector. The loop time is primarily limited by the timescale of fluctuations in the XUV source, which is discussed in further detail below.

Sample cooling for transient-absorption experiments

Many thermally sensitive chemical and condensed matter systems such as those that undergo thermal decomposition,

thermally induced phase transitions, or other temperature dependent dynamics are difficult to examine with ultrafast XUV spectroscopy in transmission mode due to the lack of heat conduction in thin-film samples. This challenge has previously been addressed by rapid sample rotation to distribute laser heating across a larger sample area.⁴⁰ We have addressed this challenge by using a stream of N_2 gas across the sample inside a gas cooling cell. A computer aided design (CAD) drawing of the gas cell is shown in Fig. 5. Two silicon nitride windows (one with the sample deposited on the side facing the gas flow, the second a blank window) are secured with face plates against the cell, and in between the membranes, N_2 gas is flown through. Gas is introduced through 1/16 in. tubing and a 250 μm diameter entrance hole in the gas cell, flown across the sample, and escapes out of the cell through a 250 μm hole at the end of the gas cell into the sample chamber. A flow rate of about 15 SCCM is used for transient absorption experiments with an estimated pressure inside the gas cell of about 10 Torr. The introduction of N_2 gas in the gas cell reduces XUV transmission by roughly 10%.

The cooling performance of the gas cell is sufficient to study the dynamics of chemical and condensed matter systems with thermal phase transitions (or other temperature-dependent dynamics) close to room temperature. In the results section, we show preliminary results of the dynamics of a Half-Heusler Ni_2MnGa sample. This particular sample undergoes a thermally induced austenite to martensite phase transition around 330 K, which can also be induced with an ultrafast laser pulse.⁴¹ With our sample cell and pumping at a modest fluence of 4 mJ/cm^2 , the sample is cooled below the phase transition temperature within 1 ms before the next pump pulse. This

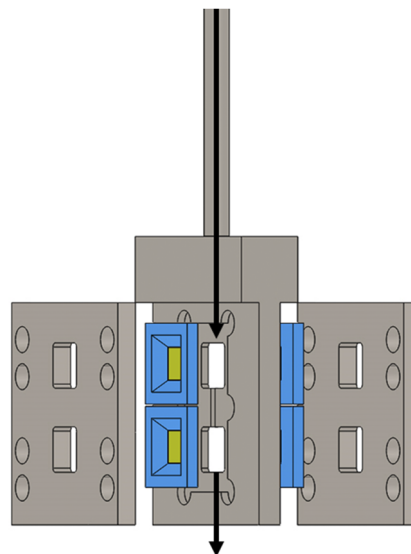


FIG. 5. Schematic of the gas cooling cell implemented in our instrument. N_2 gas is flown from a 1/16 in. tube through a small hole into a chamber sealed with silicon nitride windows. The front windows have samples deposited on the back side such that they are exposed to the N_2 gas. The gas flows over the sample and escapes through another hole at the bottom of the cell (the flow path is designated by black arrows). The main body of the cell is $13 \times 18 \text{ mm}^2$ with $5 \times 5 \text{ mm}^2$ silicon nitride membranes, as shown in the figure.

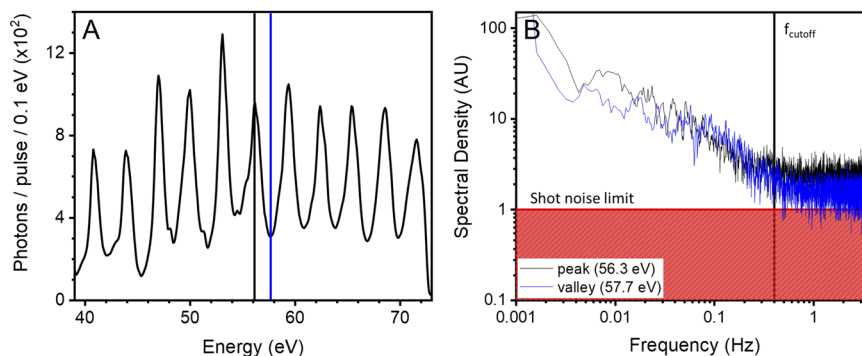


FIG. 6. (A) Flux of the XUV source at the CCD detector. (B) Noise power spectrum of the XUV source at two selected energies corresponding to the lines shown in (A).

is observed experimentally by the lack of a signal at negative delay times, which are attributed to heating dynamics on the ms timescale. To better understand the cooling capabilities of our sample cell, calculations were performed to simulate the equilibrium temperature distribution of the Ni₂MnGa transient absorption experiment performed in the next section. With the conditions used in our experiment, the maximum temperature of the sample before the next pump laser pulse is 317 K. Furthermore, details about the heat transfer calculations can be found in Appendix C. With slight modifications, this cooling method can be used with low temperature gas and enable pump-probe experiments at temperatures ranging between room temperature and 100 K.

RESULTS AND DISCUSSION

High-harmonic source output and characterization

A typical photon-corrected spectrum with Ne as the generating medium is shown in Fig. 6(A), found by using the conversion factors provided by the detector manufacturer. A continuous output from 40 to 72 eV can be obtained with a 35 fs driving laser pulse using phase matching conditions to produce harmonics with both short and long electron trajectories.^{42,43} Photon energies ranging from 30 to 120 eV can be produced with different choices of metal filters and HHG gases. Optimal conditions for absorption spectroscopy are achieved in the 40–72 eV range using a NIR pulse with an energy of 5 mJ focused 10 mm past the gas cell filled with 120 Torr Ne. The beam is apertured with an iris diaphragm of 16 mm diameter, lowering the pulse energy by less than 2%. With these generation conditions, spatial chirp arises as a consequence of the microscopic

atomic dipole phase of different quantum trajectories and, therefore, imposes a constraint of high sample homogeneity on the order of the focused beam size.^{44–46} Typical output XUV spectra have peak-to-valley ratios around 3:1. Using estimated efficiencies of the detector and grating, we approximate the flux at the source to be 3.9×10^6 and 1.5×10^6 photons/pulse at the sample. This gives an approximate energy conversion efficiency in this 32 eV window of $\sim 1 \times 10^{-8}$. We measure 1.8×10^5 photons/pulse at our detector in a 32 eV bandwidth from 40 to 72 eV, with an average of 500 photons/pulse in a 0.1 eV window (Table I). With the introduction of a thin film sample, the photons at the detector decrease by a factor of 20–50.

The spectrometer is calibrated using the Al L_{2,3}-edge at both the first and second diffraction orders, along with atomic absorption lines of xenon. The spectrometer resolution is measured with atomic Xe absorption lines and determined to be <150 meV (an example fitted Xe absorption spectrum is shown in Fig. 8 and Table II in Appendix A).

To take an absorption measurement, the transmission spectrum of a sample must be compared to a reference spectrum. If the time taken between these spectra is sufficiently long, drifts in HHG conditions can lead to large fluctuations and make the absorption measurement overly noisy. To determine the timescales of frequency dependent noise in our instrument, we collected a spectrum of the XUV source at time intervals of 80 ms for a total of 30 min. The Fourier transform yields the noise power spectrum shown in Fig. 6(B). Our XUV noise power spectra at two energies are shown, both normalized to a shot-noise limited source. In our source, the noise power spectrum exhibits ideal behavior with sampling frequencies above 0.4 Hz, which gives us a maximum

TABLE I. Overview of the characteristics of both XUV and NIR laser pulses.

Driving pulse characteristics		XUV characteristics (40–72 eV)			
Pulse length	Pulse energy	Photons/pulse at source	Photons/pulse at sample	Photons/pulse at detector	Beam size at sample (FWHM)
35 fs	5 mJ	3.9×10^6	1.5×10^6	1.8×10^5	60×49 (H \times V) μm^2

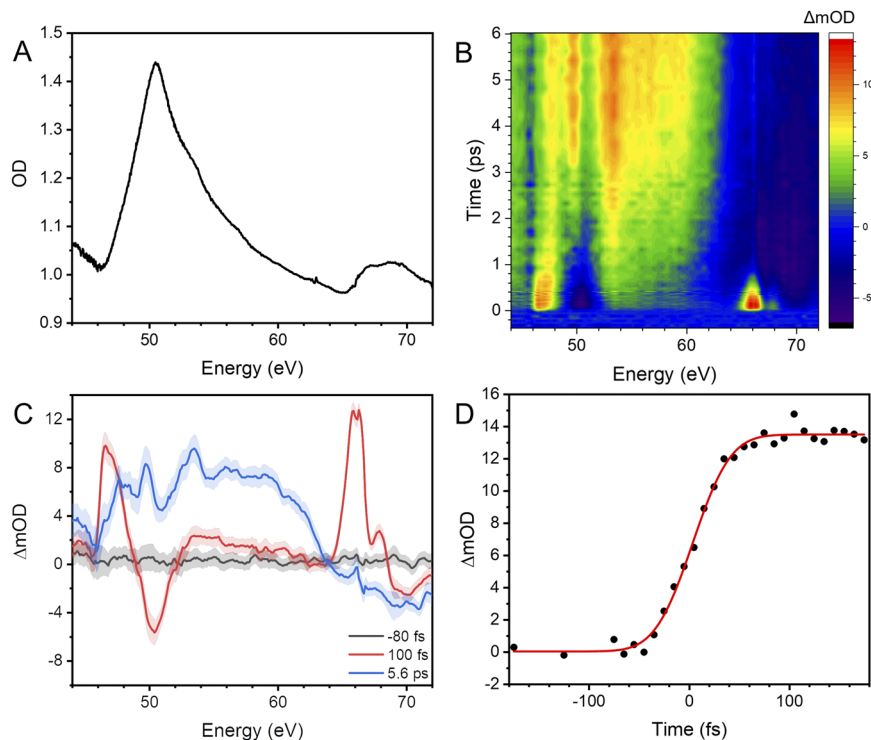


FIG. 7. (A) Static absorption spectrum of a 15 nm thick Ni_2MnGa with a 5 nm Ge cap. (B) Overview of the transient response of Ni_2MnGa after excitation at 800 nm. (C) Difference spectra at selected times representing a signal from photoexcited carriers (100 fs) and martensitic phase transitions (5.6 ps). (D) Kinetic slice of the Ni edge at 66.0 eV, showing an instrument response of 59 ± 4 fs.

sampling interval of 2.5 s. Within this sampling interval, fluctuations in the source at an energy corresponding to a harmonic peak are a factor of 2.2 above the shot-noise limit, whereas fluctuations in the valleys are only a factor of 1.6. We attribute this behavior to intensity dependent blue-shifting of the harmonic peaks.^{47–49} A singular value decomposition of harmonic spectra collected during the noise power spectrum analysis shows a major component resembling the derivative of the XUV spectrum (shown in Fig. 8 in Appendix A). This behavior, along with a correction method, has been reported previously, and we are in the process of incorporating this correction method into our instrument.⁵⁰ After this correction, we anticipate the XUV fluctuations to be a factor of 2 closer to the shot-noise limit.

Preliminary static and transient absorption measurements of Ni_2MnGa

To gain preliminary insights into the capabilities of the X-FAST instrument, we collected static and transient absorption spectra of the half-Heusler compound Ni_2MnGa . For these experiments, 15 nm thick films of $\text{Ni}_2\text{Mn}_{1.4}\text{Ga}_{0.86}$ were deposited via molecular beam epitaxy on commercially available 50 nm thick silicon nitride membranes and capped with 5 nm of amorphous Ge to prevent sample oxidation. The sample thickness and substrate material are common for XUV transmission spectroscopy and have a combined average absorbance of 1.6 in a 40–72 eV window. The sample

transmission varies less than 5% across the region rastered during transient absorption experiments.

The Heusler compound Ni_2MnGa is of interest because of its strong coupling between ferromagnetism and ferroelasticity, making it a good candidate for fundamental studies of multiferroic materials as well as a potentially applicable material for magnetic actuators, sensors, and memory devices.^{51–54} Ni_2MnGa also exhibits the shape memory effect, a phenomenon that arises from a phase transition between a cubic austenite phase and several lower symmetry martensite phases and involves interplay between structural, magnetic, and electronic properties. Despite several ultrafast experiments having been performed to study how the phase transition evolves, the mechanism of this process is not entirely understood.^{55–57}

Ultrafast XUV spectroscopy can be used to observe electronic and structural changes simultaneously at both the Ni and Mn edges after laser excitation. A static absorption spectrum of Ni_2MnGa is shown in Fig. 7(A), which is an average of 11 accumulations with a 750 ms exposure time, giving a total accumulation time (sample and reference spectra) of 16.5 s.

Transient absorption spectra of Ni_2MnGa were collected after excitation with a 55 fs, 1.8 μJ pulse centered at 800 nm. To avoid inhomogeneous sample excitation along the XUV probe, which can induce further artifacts in the spectrum, the pump size was set to $200 \pm 10 \mu\text{m}$ FWHM compared to the XUV beam size of $60 \pm 3 \times 49 \pm 2 \mu\text{m}$ ($H \times V$) FWHM. Both pump and probe beam

sizes were determined using the knife-edge scan method. The resulting pump fluence is 4 mJ/cm^2 . An overview of the dataset collected is shown in Fig. 7(B), which consists of 78 timepoints with 280 averages per timepoint. Each individual spectrum consists of 1 s accumulations of the sample with and without a pump and takes 2.5 s to acquire in the pump-probe data acquisition loop. This corresponds to an up-time of 80%, with the 20% dead time resulting from moving stages, detector readout, and writing data to a file. This results in spectra at each time point acquired in slightly under 10 min with 2σ uncertainty less than $\pm 1 \text{ mOD}$ above 60 eV. Due to lower flux in the low energy region of our spectrum, 2σ uncertainty is slightly higher at $\pm 1.5 \text{ mOD}$. With a shot-noise limited source and this sample, the same level of uncertainty would be realized in about 2.5 min of accumulation time per timepoint, given the 8500 photons/s we collect in a low flux region close to the Mn edge (48.5 eV). This is another estimate of the fluctuations in our source being slightly under two times the shot-noise limit. Overall, the dataset was accumulated over a real-time window of 18 h, split over two consecutive days. During this period, the only adjustment made to the instrument was small changes in the pump path alignment every few hours to optimize the spatial overlap of the pump and XUV beams, demonstrating the stability of the X-FAST instrument. Difference spectra with corresponding uncertainties at three selected timepoints are shown in Fig. 7(C), which show a pre- t_0 spectrum, a spectrum at 100 fs corresponding to photoexcited carriers, and finally a spectrum at 5.6 ps showing the resulting martensitic phase transition. Fitting the rise of the photoexcited carrier signal of the nickel edge at 66.0 eV shown in Fig. 7(D) results in an instrument response time of $59 \pm 4 \text{ fs FWHM}$. The temporal resolution of the instrument is currently limited by the pump pulse, as the XUV pulse is shorter than the 35 fs driving pulse and is approximated to be $< 20 \text{ fs}$.

CONCLUSION AND OUTLOOK

We have presented the design principles and preliminary data of the new X-FAST instrument, which show its viability to study ultrafast dynamics in systems of interest to physicists, chemists, and material scientists. The ability to generate high quality datasets in a reasonable time with little required input from the user is a promising step toward our goal of fully automated data collection to widen the user base of XUV spectroscopy. The next steps to fully automating the data collection system are to implement active beam stabilization of the pump, on-the-fly metrics to quantify the quality of XUV output to warn if adjustments are needed, and further safety interlocks to shut off gas flow if a failure occurs in the vacuum system. A correction method to reduce laser intensity correlated noise will also be implemented soon.

We envision future applications of the X-FAST instrument involving many users interested in the nonequilibrium dynamics of thin membrane samples, in particular, membranes subjected to extreme axial strain or tension. Large strain and strain gradients have been shown to induce exotic behavior in many systems, such as induced ferroelectricity, magnetism, and topological phase transitions.^{58–60} Studying the photoexcited dynamics of these systems has the potential to reveal even more exotic nonequilibrium states and further increase knowledge of the behavior of membranes under extreme strain.

ACKNOWLEDGMENTS

This work was in part funded by the NSF through the University of Wisconsin Materials Research Science and Engineering Center (Grant No. DMR-1720415). We acknowledge the technical staff from the Physical Science Lab and the UW Physics Machine Shop for their design help and fabrication of the X-FAST vacuum system, and the administrative staff from the UW-Madison Department of Physics. We acknowledge Phillippe Wernet, Ming-Fu Lin, and Josh Vura-Weis for helpful discussions about instrument design and John Boffard for assistance throughout the project.

AUTHOR DECLARATIONS

Conflict of Interest

The authors have no conflicts to disclose.

Author Contributions

Ryan Ash: Conceptualization (equal); Formal analysis (equal); Investigation (equal); Methodology (equal); Project administration (equal); Resources (equal); Software (equal); Supervision (equal); Validation (equal); Writing – original draft (equal); Writing – review & editing (equal). **Zain Abhari:** Formal analysis (supporting); Investigation (supporting); Resources (equal); Validation (supporting); Writing – review & editing (equal). **Roberta Candela:** Resources (equal); Software (supporting); Validation (supporting); Writing – review & editing (equal). **Noah Welke:** Resources (equal); Validation (supporting); Writing – review & editing (equal). **Jake Murawski:** Data curation (lead); Software (equal). **S. Minhal Gardezi:** Software (supporting). **Nikhilesh Venkatasubramanian:** Software (supporting). **Muneza Munawar:** Software (supporting). **Frank Siewert:** Formal analysis (supporting); Investigation (supporting); Resources (equal); Writing – review & editing (equal). **Andrey Sokolov:** Formal analysis (supporting); Investigation (supporting); Resources (equal). **Zachary LaDuca:** Resources (equal); Writing – review & editing (equal). **Jason Kawasaki:** Conceptualization (supporting); Funding acquisition (supporting); Supervision (supporting); Writing – review & editing (equal). **Uwe Bergmann:** Conceptualization (lead); Funding acquisition (lead); Project administration (lead); Supervision (lead); Writing – review & editing (equal).

DATA AVAILABILITY

The data that support the findings of this study are openly available in Figshare at <https://doi.org/10.6084/m9.figshare.23660124.v1>.

APPENDIX A: MEASURING SPECTROMETER RESOLUTION USING ATOMIC XENON

Spectrometer resolution is measured before experiments using the Rydberg 4d absorption lines in atomic xenon.⁶¹ Our spectrometer resolution cannot resolve the sixth peak in the $J = 5/2$ series and the ninth peak in the $J = 3/2$ series, so they are treated as a single line. The first five lines in the spectrum are fit with Voigt profiles using the literature values for the Lorentzian linewidth Γ , and fitting each peak's Gaussian FWHM linewidth returns the resulting spectrometer resolution. Line broadening due to other effects such

TABLE II. Results from the multi-peak fit of the Xe absorption spectrum showing the fitted peak center and Gaussian FWHM. Uncertainties are shown in parentheses.

	Peak 1	Peak 2	Peak 3	Peak 4	Peak 5
Center (eV)	65.10 (0.01)	66.36 (0.01)	66.89 (0.05)	67.08 (0.01)	68.33 (0.01)
FWHM (meV)	143 (3)	135 (6)	91 (2)	92 (4)	113 (14)

as Doppler or pressure broadening is assumed to be negligible. A step-like absorption feature after the fourth peak from continuum absorption is approximated as a wide Gaussian, which resembles an arctan-like function in the window chosen. A table showing the fitted Gaussian FWHM linewidths and uncertainties is shown beneath the absorption spectrum in Fig. 8.

APPENDIX B: ANALYSIS OF FLUCTUATIONS IN XUV BEAM

Singular value decomposition (SVD) was performed on the XUV spectra collected at 80 ms intervals over a 30 min period. The second highest weighted component of the decomposition (the first being the average of the XUV spectrum itself) has periodic derivative-like features that closely resemble the derivative of the XUV spectrum. This similarity is shown in Fig. 9. Therefore, we conclude that a primary component of the noise in our system arises from a shifting in the peak positions of the XUV source, which is known to occur with changes in laser power.^{47–49}

APPENDIX C: HEAT TRANSFER CALCULATIONS

We modeled heat transfer in a Ni₂MnGa Heusler sample as a non-linear heat transfer equation on a thin plate using MATLAB. The following equation was solved:

$$\rho c_p z \frac{\partial T}{\partial t} - kz \nabla^2 T + \sigma F(T^4 - T_R^4) = -h_c(T - T_R) - \frac{P}{2\pi\sigma_x\sigma_y} \exp\left[-\left(\frac{x^2}{2\sigma_x^2}\right) - \left(\frac{y^2}{2\sigma_y^2}\right)\right], \quad (C1)$$

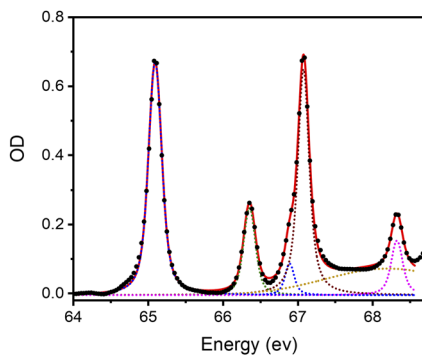


FIG. 8. Absorption spectrum of neutral xenon used for calibrating spectrometer resolution. Experimental data are shown as black dots, and the total fit to the spectrum is shown in red. Each individual component of the fit is shown as a dotted line.

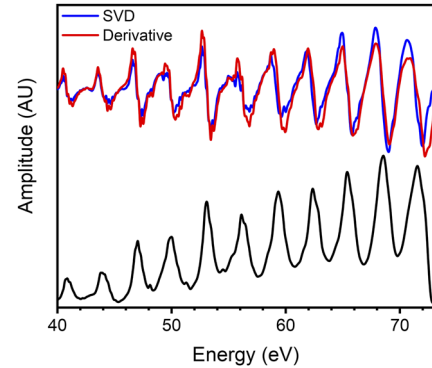


FIG. 9. Comparison of the second highest weighted component in the SVD of the XUV source fluctuation dataset (blue) compared to the derivative of the average XUV spectrum (red). The average XUV spectrum is also shown as a reference (black).

where ρ is the density, C_p is the specific heat, z is the layer thickness, T is the temperature at point (x, y) , k is the thermal conductivity, h_c is the convection coefficient, T_R is the ambient and gas temperatures, P is the absorbed average pump power, and σ is the Gaussian beam waist. The boundary conditions used to enforce the sample edges remained at 298 K, simulating efficient heat transfer from the sample frame.

To simulate the sample as a thin plate, we used a weighted sum for the thermal conductivities, specific heat capacities, and thicknesses.

The thermal coefficient values used for each layered material in the simulations can be found in Table III. Other parameters of $T_R = 298$ K, $P = 0.9$ mW (the power our sample absorbs from the 1.8 mW pump power used for the experiment), $\sigma_x = \sigma_y = 85$ μ m and $h_c = 21$ W m⁻² K⁻¹ were used. The pump beam is positioned at the sample center, where there is the minimum amount of conductive cooling, since the silicon frame supporting the membrane is much thicker. Using these parameters, the maximum sample temperature without gas cooling is 370 K, and the introduction of laser cooling reduces the max temperature to 317 K. Sample temperature distributions with and without laser cooling can be seen in Fig. 10. The convective cooling coefficient was approximated by simulating the average gas velocity in a SolidWorks flow simulation with the mass flow rate used in the experiment, then approximated using the equation

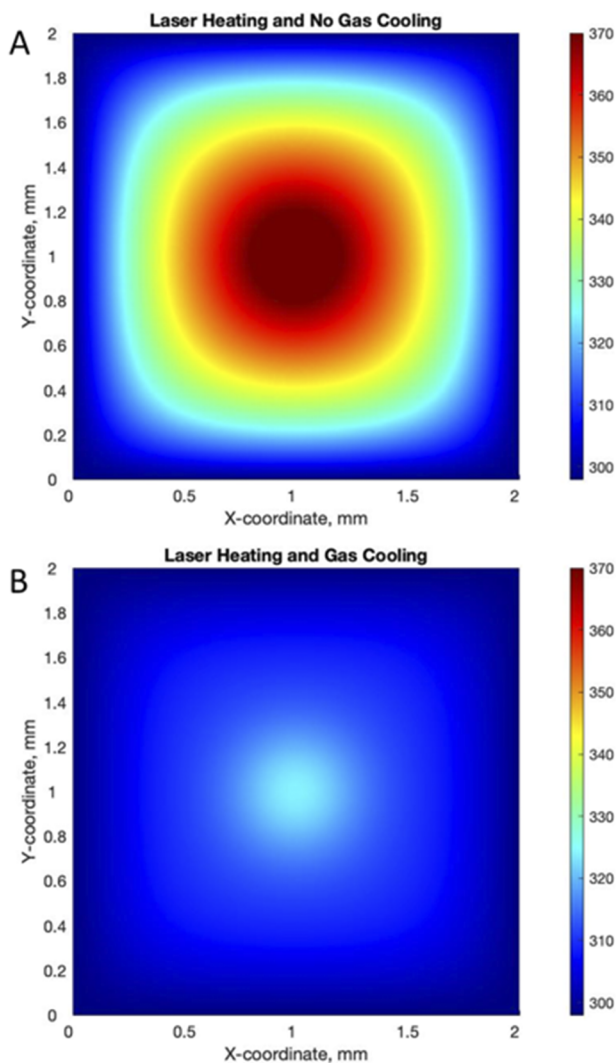
$$h_c = 12.12 - 1.16v + 11.6v^{1/2}, \quad (C2)$$

Where v is the gas velocity in m/s. Leaks in the gas cell reduce the amount of convective cooling, but our experimental evidence

TABLE III. Values used for thermal coefficients for each material used in heat transfer calculations.

Material	Silicon nitride	Ni ₂ MnGa	Germanium
ρ (kg m ⁻³)	3170	8380	5323
C_p (J kg ⁻¹ K ⁻¹)	887	550	322
z (nm)	50	15	5
k (W m ⁻¹ K ⁻¹)	30	112	64

of no thermal phase transition between laser pulses gives a lower bound on the cooling coefficient of 10 W m⁻² K⁻¹, the value at which the equilibrium temperature before the next laser pulse is 330 K.

**FIG. 10.** Temperature distribution of a Ni₂MnGa sample when excited with a 1.8 mW pump laser (a) without gas cooling and (b) with gas cooling.**REFERENCES**

- C. Bressler and M. Chergui, *Chem. Rev.* **104**, 1781 (2004).
- L. X. Chen, X. Zhang, and M. L. Shelby, *Chem. Sci.* **5**, 4136 (2014).
- P. Wernet, *Philos. Trans. R. Soc., A* **377**, 20170464 (2019).
- R. Geneaux, H. J. B. Marroux, A. Guggenmos, D. M. Neumark, and S. R. Leone, *Philos. Trans. R. Soc., A* **377**, 20170463 (2019).
- U. Bergmann, J. Kern, R. W. Schoenlein, P. Wernet, V. K. Yachandra, and J. Yano, *Nat. Rev. Phys.* **3**, 264 (2021).
- P. B. Corkum, *Phys. Rev. Lett.* **71**, 1994 (1993).
- M. Lewenstein, P. Balcou, M. Y. Ivanov, A. L'Huillier, and P. B. Corkum, *Phys. Rev. A* **49**, 2117 (1994).
- Z.-H. Loh, M. Khalil, R. E. Correa, and S. R. Leone, *Rev. Sci. Instrum.* **79**, 073101 (2008).
- L. Barreau, A. D. Ross, S. Garg, P. M. Kraus, D. M. Neumark, and S. R. Leone, *Sci. Rep.* **10**, 5773 (2020).
- F. Frassetto, A. Trabattoni, S. Anumula, G. Sansone, F. Calegari, M. Nisoli, and L. Poletto, *Rev. Sci. Instrum.* **85**, 103115 (2014).
- E. Magerl, S. Neppel, A. L. Cavalieri, E. M. Bothschafter, M. Stanislowski, T. Uphues, M. Hofstetter, U. Kleineberg, J. V. Barth, D. Menzel, F. Krausz, R. Ernstorfer, R. Kienberger, and P. Feulner, *Rev. Sci. Instrum.* **82**, 063104 (2011).
- A. D. Smith, T. Balčiūnas, Y.-P. Chang, C. Schmidt, K. Zinchenko, F. B. Nunes, E. Rossi, V. Svoboda, Z. Yin, J.-P. Wolf, and H. J. Wörner, *J. Phys. Chem. Lett.* **11**, 1981 (2020).
- C. Möller, H. Probst, J. Otto, K. Stroh, C. Mahn, S. Steil, V. Moshnyaga, G. S. M. Jansen, D. Steil, and S. Mathias, *Rev. Sci. Instrum.* **92**, 065107 (2021).
- H. T. Lemke, K. S. Kjær, R. Hartsock, T. B. van Driel, M. Chollet, J. M. Glowina, S. Song, D. Zhu, E. Pace, S. F. Matar, M. M. Nielsen, M. Benfatto, K. J. Gaffney, E. Collet, and M. Cammarata, *Nat. Commun.* **8**, 15342 (2017).
- K. S. Kjær, T. B. Van Driel, T. C. B. Harlang, K. Kunnus, E. Biasin, K. Ledbetter, R. W. Hartsock, M. E. Reinhard, S. Koroidov, L. Li, M. G. Laursen, F. B. Hansen, P. Vester, M. Christensen, K. Haldrup, M. M. Nielsen, A. O. Dohn, M. I. Pápai, K. B. Møller, P. Chabera, Y. Liu, H. Tatsuno, C. Timm, M. Jarenmark, J. Uhlig, V. Sundstöm, K. Wärnmark, P. Persson, Z. Németh, D. S. Szemes, É. Bajnóczi, G. Vankó, R. Alonso-Mori, J. M. Glowina, S. Nelson, M. Sikorski, D. Sokaras, S. E. Canton, H. T. Lemke, and K. J. Gaffney, *Chem. Sci.* **10**, 5749 (2019).
- M.-F. Lin, D. M. Neumark, O. Gessner, and S. R. Leone, *J. Chem. Phys.* **140**, 064311 (2014).
- A. S. Chatterley, F. Lackner, C. D. Pemmaraju, D. M. Neumark, S. R. Leone, and O. Gessner, *J. Phys. Chem. A* **120**, 9509 (2016).
- W. Cao, E. R. Warrick, A. Fidler, S. R. Leone, and D. M. Neumark, *Phys. Rev. A* **97**, 023401 (2018).
- F. Kelkensberg, C. Lefebvre, W. Siu, O. Ghafur, T. T. Nguyen-Dang, O. Atabek, A. Keller, V. Serov, P. Johnsson, M. Svoboda, T. Remetter, A. L'Huillier, S. Zherebtsov, G. Sansone, E. Benedetti, F. Ferrari, M. Nisoli, F. Lépine, M. F. Kling, and M. J. J. Vrakking, *Phys. Rev. Lett.* **103**, 123005 (2009).
- L. Drescher, M. C. E. Galbraith, G. Reitsma, J. Dura, N. Zhavoronkov, S. Patchkovskii, M. J. J. Vrakking, and J. Mikosch, *J. Chem. Phys.* **145**, 011101 (2016).
- E. S. Ryland, M. Lin, M. A. Verkamp, K. Zhang, K. Benke, M. Carlson, and J. Vura-Weis, *J. Am. Chem. Soc.* **140**, 4691 (2018).
- K. Zhang, R. Ash, G. S. Girolami, and J. Vura-Weis, *J. Am. Chem. Soc.* **141**, 17180 (2019).
- Y. Shari'ati and J. Vura-Weis, *Phys. Chem. Chem. Phys.* **23**, 26990 (2021).
- C. A. Leahy and J. Vura-Weis, *J. Phys. Chem. A* **126**, 9510 (2022).
- S. Biswas, J. Husek, and L. R. Baker, *Chem. Commun.* **54**, 4216 (2018).
- C. La-O-Vorakiat, E. Turgut, C. A. Teale, H. C. Kapteyn, M. M. Murnane, S. Mathias, M. Aeschlimann, C. M. Schneider, J. M. Shaw, H. T. Nembach, and T. J. Silva, *Phys. Rev. X* **2**, 011005 (2012).
- M.-F. Lin, M. A. Verkamp, J. Leveillee, E. S. Ryland, K. Benke, K. Zhang, C. Weninger, X. Shen, R. Li, D. Fritz, U. Bergmann, X. Wang, A. Schleife, and J. Vura-Weis, *J. Phys. Chem. C* **121**, 27886 (2017).

- ²⁸A. R. Attar, H.-T. Chang, A. Britz, X. Zhang, M.-F. Lin, A. Krishnamoorthy, T. Linker, D. Fritz, D. M. Neumark, R. K. Kalia, A. Nakano, P. Ajayan, P. Vashishta, U. Bergmann, and S. R. Leone, *ACS Nano* **14**, 15829 (2020).
- ²⁹M. Verkamp, J. Leveillee, A. Sharma, M.-F. Lin, A. Schleife, and J. Vura-Weis, *J. Am. Chem. Soc.* **143**, 20176 (2021).
- ³⁰S. Plogmaker, J. A. Terschlüsen, N. Krebs, M. Svanqvist, J. Forsberg, U. B. Cappel, J.-E. Rubensson, H. Siegbahn, and J. Söderström, *Rev. Sci. Instrum.* **86**, 123107 (2015).
- ³¹C. Grazioli, C. Callegari, A. Ciavardini, M. Coreno, F. Frassetto, D. Gauthier, D. Golob, R. Ivanov, A. Kivimäki, B. Mahieu, B. Bučar, M. Merhar, P. Miotti, L. Poletto, E. Polo, B. Ressel, C. Spezzani, and G. De Ninno, *Rev. Sci. Instrum.* **85**, 023104 (2014).
- ³²H. M. Watts, A. D. Smith, E. Jager, D. A. Horke, E. Springate, O. Alexander, C. Cacho, R. S. Minns, and R. T. Chapman, in *International Conference on Ultrafast Phenomena* (OSA, Washington, D.C., 2016), p. UTh4A.1.
- ³³J. R. Sutherland, E. L. Christensen, N. D. Powers, S. E. Rhynard, J. C. Painter, and J. Peatross, *Opt. Express* **12**, 4430 (2004).
- ³⁴D. S. Steingrube, T. Vockerodt, E. Schulz, U. Morgner, and M. Kovačev, *Phys. Rev. A* **80**, 043819 (2009).
- ³⁵A. Rundquist, C. G. Durfee, Z. Chang, C. Herne, S. Backus, M. M. Murnane, and H. C. Kapteyn, *Science* **280**, 1412 (1998).
- ³⁶S. Kazamias, F. Weihe, D. Douillet, C. Valentin, T. Planchon, S. Sebban, G. Grillon, F. Augé, D. Hulin, and P. Balcou, *Eur. Phys. J. D* **21**, 353 (2002).
- ³⁷T. Kita, T. Harada, N. Nakano, and H. Kuroda, *Appl. Opt.* **22**, 512 (1983).
- ³⁸B. L. Henke, E. M. Gullikson, and J. C. Davis, *At. Data Nucl. Data Tables* **54**, 181 (1993).
- ³⁹F. Schäfers, P. Bischoff, F. Eggenstein, A. Erko, A. Gaupp, S. Künstner, M. Mast, J.-S. Schmidt, F. Senf, F. Siewert, A. Sokolov, and T. Zeschke, *J. Synchrotron Radiat.* **23**, 67 (2016).
- ⁴⁰M. F. Jager, C. Ott, C. J. Kaplan, P. M. Kraus, D. M. Neumark, and S. R. Leone, *Rev. Sci. Instrum.* **89**, 013109 (2018).
- ⁴¹X. Xu, M. Nagasako, W. Ito, R. Y. Umetsu, T. Kanomata, and R. Kainuma, *Acta Mater.* **61**, 6712 (2013).
- ⁴²P. Salières, A. L'Huillier, and M. Lewenstein, *Phys. Rev. Lett.* **74**, 3776 (1995).
- ⁴³M. Lewenstein, P. Salières, and A. L'Huillier, *Phys. Rev. A* **52**, 4747 (1995).
- ⁴⁴C. Lyngå, M. B. Gaarde, C. Delfin, M. Bellini, T. W. Hänsch, A. L' Huillier, and C.-G. Wahlström, *Phys. Rev. A* **60**, 4823 (1999).
- ⁴⁵T. Auguste, P. Salières, A. S. Wyatt, A. Monmayrant, I. A. Walmsley, E. Cormier, A. Zaïr, M. Holler, A. Guandalini, F. Schapper, J. Biegert, L. Gallmann, and U. Keller, *Phys. Rev. A* **80**, 033817 (2009).
- ⁴⁶M.-F. Lin, M. A. Verkamp, E. S. Ryland, K. Zhang, and J. Vura-Weis, *J. Opt. Soc. Am. B* **33**, 1986 (2016).
- ⁴⁷H. J. Shin, D. G. Lee, Y. H. Cha, K. H. Hong, and C. H. Nam, *Phys. Rev. Lett.* **83**, 2544 (1999).
- ⁴⁸M. Geissler, G. Tempea, and T. Brabec, *Phys. Rev. A* **62**, 033817 (2000).
- ⁴⁹C. Altucci, R. Bruzzese, C. de Lisio, M. Nisoli, S. Stagira, S. De Silvestri, O. Svelto, A. Boscolo, P. Ceccherini, L. Poletto, G. Tondello, and P. Villoresi, *Phys. Rev. A* **61**, 021801 (1999).
- ⁵⁰M. Volkov, J. Pupeikis, C. R. Phillips, F. Schlaepfer, L. Gallmann, and U. Keller, *Opt. Express* **27**, 7886 (2019).
- ⁵¹K. Ullakko, J. K. Huang, C. Kantner, R. C. O'Handley, and V. V. Kokorin, *Appl. Phys. Lett.* **69**, 1966 (1996).
- ⁵²V. A. Chernenko and S. Besseghini, *Sens. Actuators, A* **142**, 542 (2008).
- ⁵³I. Karaman, B. Basaran, H. E. Karaca, A. I. Karsilayan, and Y. I. Chumlyakov, *Appl. Phys. Lett.* **90**, 172505 (2007).
- ⁵⁴S. P. Venkateswaran, N. T. Nuhfer, and M. De Graef, *Acta Mater.* **55**, 5419 (2007).
- ⁵⁵S. O. Mariager, C. Dornes, J. A. Johnson, A. Ferrer, S. Grübel, T. Huber, A. Caviezel, S. L. Johnson, T. Eichhorn, G. Jakob, H. J. Elmers, P. Beaud, C. Quitmann, and G. Ingold, *Phys. Rev. B* **90**, 161103 (2014).
- ⁵⁶S. O. Mariager, A. Caviezel, P. Beaud, C. Quitmann, and G. Ingold, *Appl. Phys. Lett.* **100**, 261911 (2012).
- ⁵⁷S. Schwabe, K. Lünser, D. Schmidt, K. Nielsch, P. Gaal, and S. Fähler, *Sci. Technol. Adv. Mater.* **23**, 633 (2022).
- ⁵⁸R. Xu, J. Huang, E. S. Barnard, S. S. Hong, P. Singh, E. K. Wong, T. Jansen, V. Harbola, J. Xiao, B. Y. Wang, S. Crossley, D. Lu, S. Liu, and H. Y. Hwang, *Nat. Commun.* **11**, 3141 (2020).
- ⁵⁹D. Du, S. Manzo, C. Zhang, V. Saraswat, K. T. Genser, K. M. Rabe, P. M. Voyles, M. S. Arnold, and J. K. Kawasaki, *Nat. Commun.* **12**, 2494 (2021).
- ⁶⁰C. Lin, M. Ochi, R. Noguchi, K. Kuroda, M. Sakoda, A. Nomura, M. Tsubota, P. Zhang, C. Bareille, K. Kurokawa, Y. Arai, K. Kawaguchi, H. Tanaka, K. Yaji, A. Harasawa, M. Hashimoto, D. Lu, S. Shin, R. Arita, S. Tanda, and T. Kondo, *Nat. Mater.* **20**, 1093 (2021).
- ⁶¹D. L. Ederer and M. Manalis, *J. Opt. Soc. Am.* **65**, 634 (1975).